Journal of Materials Chemistry A

ROYAL SOCIETY OF CHEMISTRY

PAPER

View Article Online
View Journal | View Issue

Cite this: J. Mater. Chem. A, 2025, 13, 28409

A perovskite nanocomposite and self-assembled nanoparticle-decorated cathode for low temperature SOFCs

Chunyang Yang, Gang Wang and Xingjian Xue *

One-pot route synthesis of an A-site Sm-doped simple perovskite with nominal composition $Sm_{0.10}Ba_{0.90}Co_{0.8}Fe_{0.2}O_{3-\delta}$ leads to a novel perovskite nanocomposite containing ~90% A-site cation deficient cubic simple perovskite $Ba_{0.925}(Co/Fe)_{0.962}Sm_{0.038}O_{3-\delta}$ and ~10% orthorhombic layered perovskite $SmBa(Co/Fe)_2O_{5+\delta}$. The synergy of the two phases in the nanocomposite results in high electrochemical kinetic properties at low temperatures. With the novel perovskite nanocomposite, a surface nanoparticle-decorated nanocomposite cathode is self-assembled through a one-step sintering process. The corresponding anode-supported cell delivers a peak power density of 1271 mW cm^{-2} at 650 °C. The cell also demonstrates long-term stability (~333 h) under a current load of 600 mA cm^{-2} and shows short-term stability (~16 h) under an alternating large current load between 600 and 1700 mA cm^{-2} at 600 °C. The novel perovskite nanocomposite developed in this paper is among the best in open literature for cathodes of low temperature SOFCs.

Received 18th May 2025
Accepted 17th July 2025

DOI: 10.1039/d5ta03982g

rsc.li/materials-a

1 Introduction

Solid oxide fuel cells (SOFCs) have attracted considerable attention due to their high efficiency, low pollutant emission, and fuel flexibility.[1–3] The early stage SOFC technologies usually operate under high temperature conditions (>850 °C). While high operating temperatures may improve electrochemical kinetics, they also cause high system and operating costs, various forms degradation, and limited selection of materials and components for the system.[4,5] To mitigate these issues while widening the selection of less expensive materials, *e.g.*, metallic interconnects, intermediate temperature SOFC (IT-SOFC, 650–800 °C) technologies have been widely pursued over the past decade.[5,6] Reducing operating temperature of SOFCs may also bring other advantages of enabling readily sealing and quick start-up and shut-down of the system and potential applications for portable devices and transportations.[4,5,7] To further enhance advantages induced by reducing operating temperatures, low temperature SOFC (LT-SOFCs, less than 650 °C) technologies have been extensively studied in recent years. Nevertheless, lowering operating temperature usually leads to lower electrochemical performance of SOFCs compared to their high temperature counterparts. In particular, the bulk diffusion and surface exchange processes are thermally activated in nature. When the operating temperature decreases, it deteriorates SOFC performance. Since the cathode electrode is a dominant component affecting SOFC performance, it is critical to develop high performance cathodes for LT-SOFCs.[8]

One strategy to achieve high performance cathodes is to develop novel cathode materials that have excellent properties of electrochemical kinetics at relatively low temperatures. ABO_3-type simple perovskites have been widely studied as mixed ionic and electronic conducting (MIEC) cathode materials for SOFCs. Typically, relatively large size alkaline-earth metal elements are used in the A-sites while relatively small size transition metal elements are utilized in the B-sites. Such versatility allows ABO_3 perovskites to tune phase structures and electrochemical kinetic properties simultaneously. In particular, the combination of large ions (*e.g.*, Ba and Sr) at A-sites and small ions (*e.g.*, Co and Fe) at B-sites may create sufficient lattice free volume and oxygen vacancies. These will lead to relatively low activation energy, facilitating oxygen ion migration in the perovskite lattice at relatively low temperatures. In addition, suitable doping of large ions at A-sites and small ions at B-sites may tune the Goldschmidt tolerance factor of crystal structures close to unity, creating highly symmetrical simple cubic phases. The symmetrical cubic phase in turn enables isotropic 3-D oxygen ion diffusion, enhancing ionic conductivity.[9,10] On the other hand, driven by the creation of oxygen vacancies, the valence state of transition metal elements at B-sites will change to maintain charge neutrality of the crystal structures. The variations of valances and spin states of transition elements at B-sites are largely related to the (electro) catalytic properties of the material. In this context, a class of $ABO_{3-\delta}$ type MIECs has been extensively studied as cathode materials for SOFCs. Typically, different doping strategies are applied to the parent

Department of Mechanical Engineering, University of South Carolina, Columbia, SC 29208, USA. E-mail: Xue@cec.sc.edu; Fax: +1-803-777-0106; Tel: +1-803-576-5598

compositions of $BaCoO_{3-\delta}$ and $SrCoO_{3-\delta}$ so that their properties are improved such as electrochemical kinetics and stability.[11–13] Unfortunately, the electrical conductivities are relatively low in the range of intermediate to low temperatures especially for Ba-containing simple perovskites. For instance, in the temperature range of 300–800 °C, $(Ba_{0.5}Sr_{0.5})_{0.91}Co_{0.8}Fe_{0.2}O_{3-\delta}$ shows an electrical conductivity of 9.7–26.6 S cm^{-1} and $Ba_{0.95}Co_{0.7}Fe_{0.2}Nb_{0.1}O_{3-\delta}$ demonstrates 2.2–10.2 S cm^{-1},[12,14] while the recently studied low temperature cathode material $BaCo_{0.4}Fe_{0.4}Zr_{0.1}Y_{0.1}O_{3-\delta}$ displays an electrical conductivity of 0.4–2.2 S cm^{-1}.[15] To obtain a reasonably good performance of LT-SOFCs, the electronic conductivity of the cathode material in conjunction with a suitable current collector should be greater than 100 S cm^{-1} at ~600 °C.[7] Therefore, electronic conductivity of simple perovskites should be further improved when used for LT-SOFCs. In open literature, A-site ordered layered perovskites with the general chemical formula $AA'B_2O_6$ have also been extensively studied as cathode materials for SOFCs. $AA'B_2O_6$ perovskites stack A- and A′-layers alternately along the *c*-axis with rare-earth ions or Y at A-sites and alkaline-earth ions at A′-sites. The B-sites are usually occupied by transition-metal ions. Oxygen vacancies are confined within the A-layers, as is oxygen ion transport. Compared to isotropic oxygen ionic transport in a cubic ABO_3 simple perovskite, this anisotropic transport channel has disadvantages for facile oxygen ion diffusion in a bulk cathode with polycrystals in different orientations. Interestingly, A-site ordered layered perovskites usually demonstrate relatively high electrical conductivity at intermediate temperatures. For example, the electrical conductivity of $SmBaCo_2O_{5+\delta}$ may reach 500–800 S cm^{-1} at 600 °C.[16,17] Therefore, a composite material combining a simple perovskite with an A-site ordered layered perovskite may bring advantages of both facile oxygen ion transport and high electronic conduction for high performance cathodes. To take full advantage of synergetic effects the two materials can bring, it is crucial to composite them at nanoscales with a high uniformity.

Another strategy to obtain high performance cathodes at low temperatures is through nano/microstructure innovation of cathode electrodes. The widely used method is precursor solution infiltration, where the precursor solution is infiltrated into the porous backbone of a cathode electrode.[18] After heat treatment at relatively low temperature (700–850 °C), the phase is formed and bonded onto the backbone as nanoparticles, forming nanostructured cathodes. The surface nanoparticles may significantly improve effective surface area for the ORR, achieving a high performance cathode. The infiltration strategy provides the flexibility of combining different phases to form a nanostructured cathode. Since the surface phase can be formed at a relatively low firing temperature, undesired chemical reactions can be avoided between the infiltrated phase and the backbone. To obtain sufficient loading and uniform surface nanoparticles, it usually requires multiple times infiltration. Depending on the thickness and porous structure features of the cathode, up to 7–10 times are needed.[18] Also, only relatively simple phases can be obtained. When the composition of the surface phase is complicated, it is difficult to get pure phases and impurity phases could occur on the surface of the backbone. Alternatively, an exsolution approach is also employed to create novel electrodes arched with surface metal nanoparticles.[19] The metal ions are first doped into the crystals of electrode materials, typically MIECs. When the electrode is subject to a reducing atmosphere at elevated temperatures, some of the doped metal ions are exsolved onto the surface of the parent material, forming metal nanoparticles arched on the surface of the electrode backbone. Such a nanostructured electrode significantly improves effective surface area and surface catalytic properties, therefore resulting in a high performance electrode. This fabrication process implies that the parent materials should have certain stability in reducing atmospheres at elevated temperatures. Also, to avoid oxidation of exsolved surface metal nanoparticles and thus deterioration of surface catalytic properties, either a reducing atmosphere should be maintained under operating conditions or the exsolved metal nanoparticles should have anti-oxidation properties in an oxidizing atmosphere at elevated temperatures. The former case has been widely used for the fabrication of nanostructured anode electrodes. While the latter case could be employed for nanostructured cathode fabrication, the exsolved nanoparticles must be anti-oxidants such as precious metals, Ag, Pt, and $Sr_{0.95}Ag_{0.05}Nb_{0.1}Co_{0.9}O_{3-\delta}$.[20] Because of this limitation, very few cases can be found in the literature for nanostructured cathode fabrication using the exsolution method. From the above simple overview, one can see that multiple steps are needed for surface nanoparticle decorated cathode fabrication when infiltration and/or exsolution methods are employed. Furthermore, only relatively simple phases of surface nanoparticles could be obtained. Therefore, innovation is needed to create nanostructured cathodes by a simple route and surface nanoparticles are not limited to simple phases, which can promote cathode performance at low temperatures.

Inspired by the above understanding of cathode materials and associated nanostructures, in this research, novel perovskite nanocomposites with nominal composition $Sm_xBa_{1-x}Co_{0.8}Fe_{0.2}O_{3-\delta}$ ($x = 0$, 0.05, 0.10, 0.15 and 0.30) were studied as potential cathode materials for LT-SOFCs. The nanocomposite was synthesized using a one-pot route. Depending on Sm doping levels, nanocomposites may contain different amounts of simple perovskites with cubic/hexagonal phases and layered perovskites with orthorhombic symmetry. Among these nanocomposites, the nominal composition $Sm_{0.1}Ba_{0.9}Co_{0.8}Fe_{0.2}O_{3-\delta}$ led to the best ORR activity since it consists primarily of an A-site cation deficient $Ba_{1-x}(Co/Fe)O_{3-\delta}$ type simple perovskite with cubic symmetry and minor layered perovskite $SmBa(Co/Fe)_2O_{5+\delta}$ with orthorhombic symmetry. The synergy of the two phases may result in advantages of high electrical conductivity, bulk diffusivity and surface exchange coefficients.[21,22] The crystal structures, compositions and phase ratio in the nanocomposite were characterized and quantitatively determined using element balance equations of chemical synthesis reactions in combination with the XRD technique and Rietveld refinement. The nanocomposite was further characterized and verified using SEM and TEM techniques. Electrochemical kinetic properties such as conductivity, surface

exchange coefficient, bulk diffusivity, and polarization were obtained using various techniques. Cathodic processes associated with the nanocomposite were identified. The long-term stability of the nanocomposite as a cathode was also characterized by using a symmetrical cell test. The synthesized nanocomposite was then used to fabricate a cathode electrode, and surface nanoparticles were self-assembled and decorated onto the surface of the cathode backbone during the one-step sintering process. The electrochemical performance of an anode-supported button cell with the nanoparticle-decorated nanocomposite cathode was measured and characterized. The stability of the cell was also studied under both a constant and an alternating large current loading (between 600 and 1700 mA cm^{-2}). The phases and microstructure of the post-test cathode were characterized and analyzed. The corresponding degradations were analyzed and discussed.

2 Experimental

2.1 Powder synthesis

The powders with nominal composition $Sm_xBa_{1-x}Co_{0.8}Fe_{0.2}O_{3-\delta}$ ($x = 0$, 0.05, 0.10, 0.15 and 0.30, simply denoted as Sm0BCF, Sm5BCF, Sm10BCF, Sm15BCF and Sm30BCF, respectively) were synthesized *via* a combined ethylenediaminetetraacetic (EDTA) and citric acid complexing method. Stoichiometric amounts of $Sm(NO_3)_3 \cdot 6H_2O$ (Alfa Aesar, 99.99%), $Ba(NO_3)_2$ (Alfa Aesar, 99.999%), $Co(NO_3)_2 \cdot 6H_2O$ (Alfa Aesar, 99.99%) and $Fe(NO_3)_3 \cdot 9H_2O$ (Alfa Aesar, 99.99%) were used as raw materials for the necessary metal ions. EDTA and citric acid were used as complexing agents. A molar ratio of citric acid:EDTA:metal ions = 1.5 : 1 : 1 was employed. Ammonia was used to adjust the pH of the solution to ~8. After mixing homogeneously, the solution was dehydrated at 80 °C to form a gel, which was then burned on an electrical heater until it combusted to form a bouffant precursor powder. Subsequently, the precursors were ground, followed by calcining at 400 °C in air for 2 h to remove organic residues. Finally, the powders were heat-treated at 1000 °C in air for 6 h to achieve the desired phases.

2.2 Sample preparation

A cuboid Sm10BCF bar was fabricated for electrical conductivity and electrical conductivity relaxation (ECR) measurement. Specifically, Sm10BCF powder was ground with a PVB binder (2 wt%) and uniaxially pressed using a stainless-steel mold, followed by sintering at 1100 °C in air for 6 h. The surface of the sample bars was mechanically polished with sandpaper, followed by washing using ethanol with an ultrasonic cleaner. Four silver wires were attached at well-aligned different locations on the surface of the sample bars using Ag paste (Heraeus 2807).

The $Ce_{0.8}Sm_{0.2}O_{1.9}$ (SDC) electrolyte powder (tape cast grade, Fuel Cell Material, USA) was mixed and ground thoroughly with the PVB binder (2 wt%) in ethanol. After drying, the electrolyte powder was dry pressed to form pellets, which were then densified by sintering at 1450 °C in air for 6 h. The surface of the dense pellets was then polished using sandpaper, followed by cleaning using an ultrasonic machine. Symmetrical cells with the configuration of $Sm_xBa_{1-x}Co_{0.8}Fe_{0.2}O_{3-\delta}$/SDC/$Sm_xBa_{1-x}Co_{0.8}Fe_{0.2}O_{3-\delta}$ were fabricated for electrochemical impedance spectroscopy (EIS) measurements. Specifically, the cathode slurry was first prepared by mixing cathode powders with a binder (α-terpineol solution of 6 wt% ethylene cellulose) in a weight ratio of 2 : 1. The prepared slurry was then symmetrically screen-printed onto both sides of the dense SDC electrolyte pellets followed by annealing at 1050 °C in air for 2 h. A thin layer of Ag paste was then painted onto the electrode surfaces and silver wires were attached onto the surfaces, which served as current collectors.

The anode-supported single cell NiO + SDC/SDC/Sm10BCF was fabricated for electrochemical and stability tests. Specifically, the powders of NiO (fine grade, Fuel Cell Material, USA) and SDC and starch with a weight ratio of 60 : 40 : 20 were mixed and ball-milled in ethanol for 24 h. After drying, the well mixed anode powder was mechanically pressed and pre-sintered at 1100 °C in air for 3 h to form anode green pellets. SDC powder was mixed with a dispersant (triethanolamine), plasticizers (di-*n*-butyl phthalate and polyethylene glycol), and a binder (polyvinyl butyral). The mixture was ball-milled in ethanol to form a homogeneous spinning slurry. The as-prepared SDC electrolyte slurry of 80 μL was drop-coated onto the surface of the green anode pellets. The pellets were then dried in air for 6 h followed by pre-sintering at 800 °C in air for 2 h. This drop-coating and pre-sintering process was repeated two times to obtain SDC electrolyte with sufficient thickness. The electrolyte was then densified by sintering at 1450 °C in air for 6 h and anode-supported half-cell NiO-SDC/SDC was obtained. The anode thickness of the half-cell was reduced to ~0.5 mm by grinding. The Sm10BCF cathode slurry prepared above was then applied onto the electrolyte surface using screen printing followed by sintering at 1050 °C in air for 2 h. Ag paste was applied to both the anode and cathode electrodes, which served as current collectors.

2.3 Measurement and characterization

The phase analysis was performed using X-ray diffraction (XRD, Rigaku) with Cu Kα ($\lambda = 1.5406$ Å) at room temperature using a step size of 0.02° in the range of $10° \leq 2\theta \leq 90°$. The morphology of Sm10BCF powder was characterized by transmission electron microscopy (TEM) measurements (Hitachi H-9500 TEM with an accelerating voltage of 300 kV). To prepare samples for TEM measurements, Sm10BCF powder was diluted in ethanol and sonicated for 30 min to ensure homogeneous distribution of particles. Two drops of the suspension were deposited onto a carbon-stabilized formvar copper grid and completely dried at room temperature prior to measurement. The microstructures of the samples were examined using scanning electron microscopy (SEM, Zeiss Ultra Plus FESEM, Germany) in combination with energy-dispersive X-ray spectroscopy (EDS).

Electrical conductivity of the Sm10BCF sample bar was measured using a four-terminal DC method. The temperature

of the sample bar was controlled by a tube furnace. For a given operating temperature, electrical conductivity of the sample bar was monitored using a digital multimeter (Agilent 34401A) until an equilibrium was reached and the corresponding conductivity was recorded. The electrical conductivity measurement was conducted at every temperature difference of 50 °C between 700 and 250 °C. Electrical conductivity relaxation (ECR) measurement was also performed to determine the surface exchange coefficient (k) and bulk diffusivity (D) of the Sm10BCF material. Specifically, the Sm10BCF sample bar with the silver wire assembly was sealed in an alumina test chamber. The chamber temperature was controlled by a high temperature tube furnace. A gas mixture of oxygen and nitrogen was supplied to the test chamber. The conductivity of the sample bar was automatically recorded using a digital multimeter (Agilent, 34401A) in combination with a computer system. The gas mixture with an oxygen partial pressure of 0.21 atm was first supplied into the chamber. After the conductivity reached an equilibrium state, a step-change of oxygen partial pressure from 0.21 atm to 0.1 atm was applied to the supplied gas mixture. The corresponding transient response of electrical conductivity was recorded until it reached a new equilibrium. The surface exchange coefficient and bulk diffusivity were then extracted from ECR data using a curve-fitting technique.[23]

Electrochemical impedance spectra (EIS) of the symmetrical cell with the $Sm_xBa_{1-x}Co_{0.8}Fe_{0.2}O_{3-\delta}$ electrode were measured using a Zahner IM6E electrochemical workstation. The measurement was conducted in air under open circuit voltage (OCV) conditions in the temperature range of 500 to 650 °C. The EIS was obtained in the frequency range from 10^6 to 0.1 Hz with a voltage perturbation of 10 mV. To further investigate the ORR process of the Sm10BCF cathode, polarization resistances were measured using the symmetrical cell Sm10BCF/SDC/Sm10BCF. The symmetrical cell was sealed in an alumina chamber. The temperature of the alumina chamber was controlled by a tube furnace. A mixture of oxygen and nitrogen with different $O_2:N_2$ ratios was supplied into the chamber so that different oxygen partial pressures were applied to the symmetrical cell. The EIS of the symmetrical cell at different oxygen partial pressures and temperatures was obtained. The stability of Sm10BCF as a cathode material was tested in air at 600 °C for ~200 h using the symmetrical cell of Sm10BCF/SDC/Sm10BCF. During the test, the EIS was periodically measured, and the time history of polarization resistance was obtained. The anode-supported button cell was sealed on an alumina tube using a ceramic binder (Aremco Products, Inc., USA). The temperature of the alumina tube-supported cell was controlled by a vertical split furnace. Humidified hydrogen as fuel was supplied into the anode alumina supporting tube while the cathode was exposed to ambient air. I–V polarization curves were measured under a hydrogen flow rate of 80 mL min^{-1} over the temperature range from 550 to 650 °C. The stability test of the button cell was performed under a current density load of 600 mA cm^{-2} for 333 h. The stability test of the cell was also conducted under a very large current load for about 16 h, where the current density load was changed between 600 and 1700 mA cm^{-2} alternately every two hours. The time history of cell voltage was recorded.

3 Results and discussion

3.1 Crystal structure

The crystal structures of powder materials with the nominal composition of $Sm_xBa_{1-x}Co_{0.8}Fe_{0.2}O_{3-\delta}$ (x = 0, 0.05, 0.1, 0.15 and 0.3) were characterized by XRD and are shown in Fig. 1a. It is clear to see that XRD patterns change upon Sm doping levels. To understand the involved phases and structure evolution induced by Sm doping levels, the undoped sample with the nominal composition of $BaCo_{0.8}Fe_{0.2}O_{3-\delta}$ was first examined. It

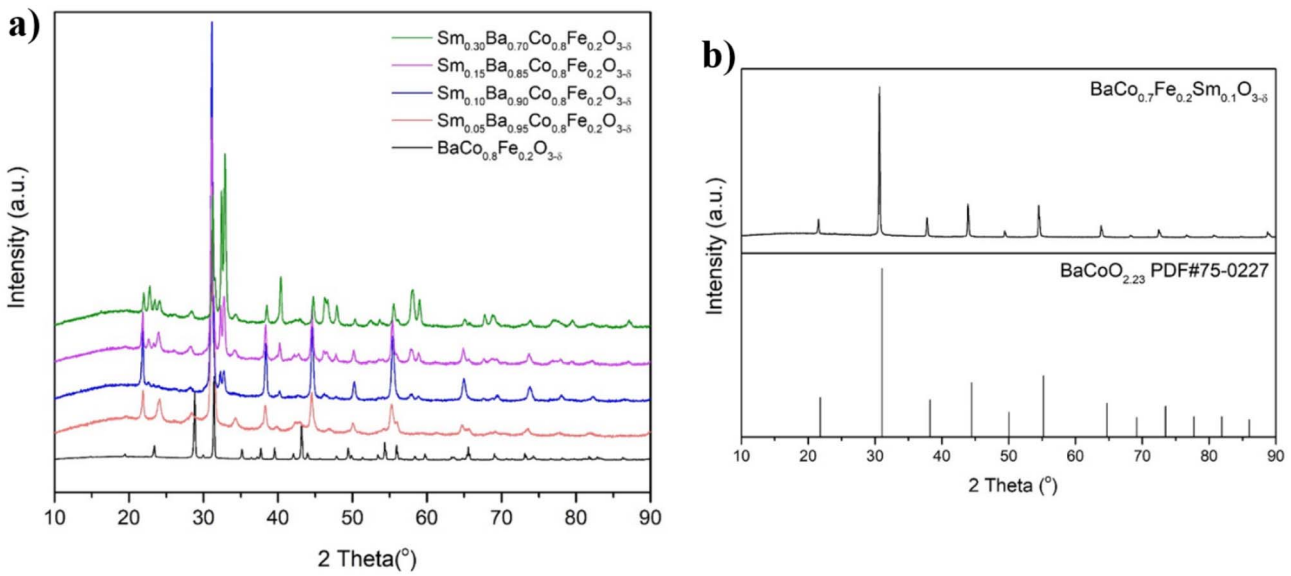

Fig. 1 XRD patterns of (a) $Sm_xBa_{1-x}Co_{0.8}Fe_{0.2}O_{3-\delta}$ (x = 0, 0.05, 0.1, 0.15 and 0.3) powders and (b) $BaCo_{0.7}Fe_{0.2}Sm_{0.1}O_{3-\delta}$ powder calcined at 1000 °C in air for 6 h.

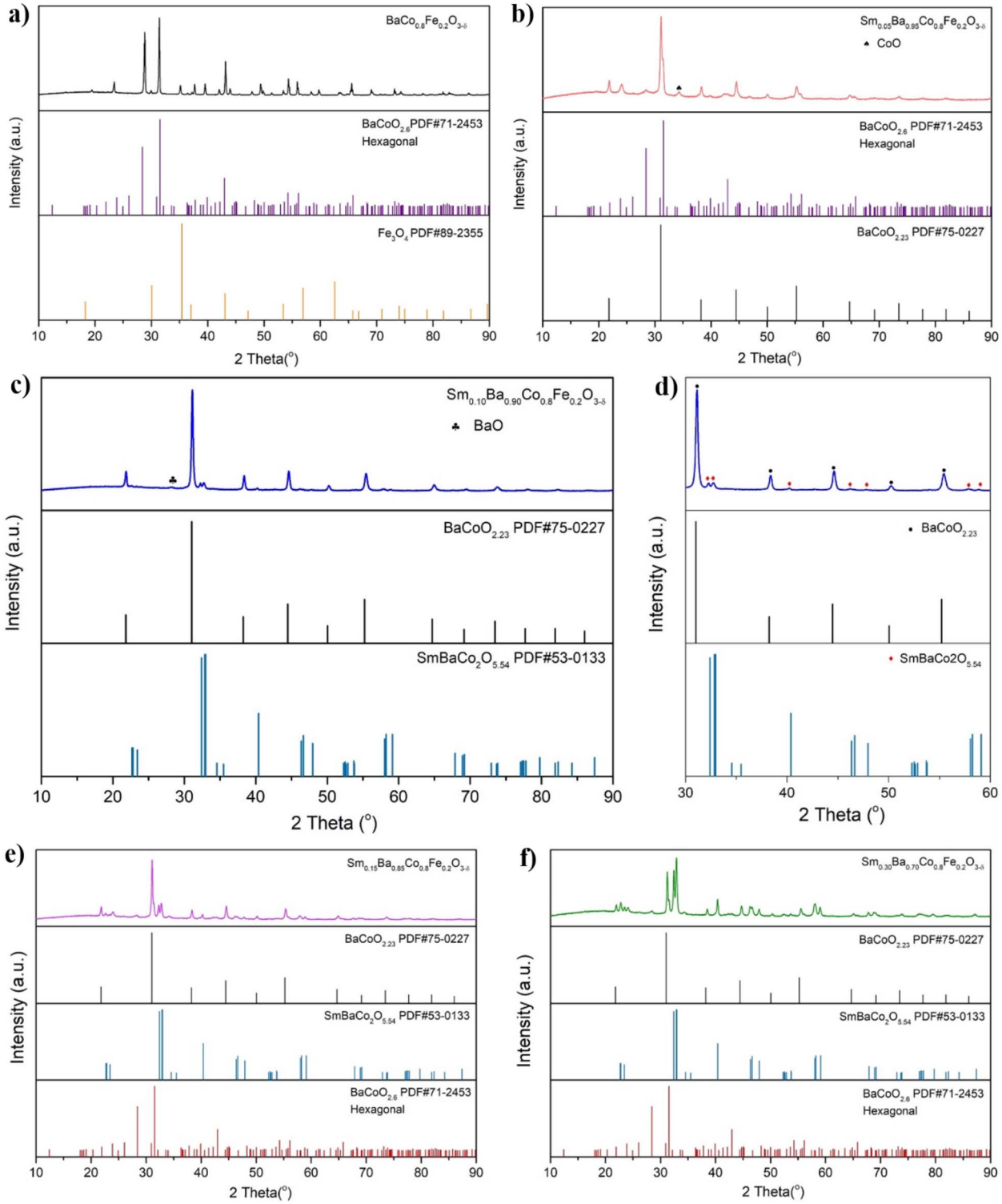

Fig. 2 XRD patterns of powders calcined at 1000 °C in air for 6 h. (a) $BaCo_{0.8}Fe_{0.2}O_{3-\delta}$; peak positions of hexagonal phase $BaCoO_{2.6}$ and Fe_3O_4. (b) $Sm_{0.05}Ba_{0.95}Co_{0.8}Fe_{0.2}O_{3-\delta}$; peak positions of hexagonal phase $BaCoO_{2.6}$, cubic phase $BaCoO_{2.23}$ and CoO. (c) $Sm_{0.10}Ba_{0.90}Co_{0.8}Fe_{0.2}O_{3-\delta}$; peak positions of cubic phase $BaCoO_{2.23}$ and orthorhombic phase $SmBaCo_2O_{5.54}$. (d) $Sm_{0.10}Ba_{0.90}Co_{0.8}Fe_{0.2}O_{3-\delta}$; a magnified pattern of 2θ = 30–60°. (e and f) $Sm_{0.15}Ba_{0.85}Co_{0.8}Fe_{0.2}O_{3-\delta}$, $Sm_{0.30}Ba_{0.70}Co_{0.8}Fe_{0.2}O_{3-\delta}$, peak positions of cubic phase $BaCoO_{2.23}$, orthorhombic phase $SmBaCo_2O_{5.54}$ and hexagonal phase $BaCoO_{2.6}$.

can be seen from Fig. 2a that the undoped sample was crystallized into a hexagonal phase of $BaCoO_{2.6}$ and an impurity phase of Fe_3O_4. Upon substitution of Ba by 5 mol% Sm (Sm5BCF), the synthesized powders are primarily composed of hexagonal phases of simple perovskite $BaCoO_{2.6}$ and cubic phase $BaCoO_{2.23}$, and a minor phase of CoO also emerges as shown in

Fig. 2b. The appearance of a cubic phase could be induced by Sm doping, partially substituting Ba on A-sites and/or (Co, Fe) on B-sites. At this stage, the exact composition of the resultant simple perovskite is not known, which is simply denoted as (Ba/Sm)(Co/Fe/Sm)$O_{3-\delta}$. On increasing the Sm doping amount to 10 mol%, two major phases can be identified as shown in Fig. 2c. One is a simple perovskite phase with cubic symmetry and another is a layered perovskite phase $SmBa(Co/Fe)_2O_{5+\delta}$ with orthorhombic symmetry. A very small amount of BaO (PDF#74-1228) can also be observed at around 28° and is marked in Fig. 2c. The magnified XRD patterns in the range of $2\theta = 30$–60° shown in Fig. 2d further confirm that the peaks of the Sm10BCF sample correspond to the three phases mentioned above. On increasing the Sm amount to 15 mol%, the simple perovskite and layered perovskite were formed, and the simple perovskite includes both the hexagonal phase and cubic phase (Fig. 2e). A relatively higher amount of double perovskite can be found in Sm15BCF than in Sm10BCF (see Fig. 2e and c). The amount of double perovskite further increased for Sm30BCF as shown in Fig. 2f. Table 1 summarizes various phases contained in Sm*x*BCF nanocomposites.

The observations from the above XRD characterization studies indicate that very complicated phase evolution occurred for the nominal composition $Sm_xBa_{1-x}Co_{0.8}Fe_{0.2}O_{3-\delta}$ with an increasing Sm doping level from $x = 0$ to 0.3. Simple perovskites with both hexagonal and cubic phases were formed at $x = 0.05$. Once the Sm doping level reached $x = 0.1$, both the simple perovskite with cubic symmetry and layered perovskite with orthorhombic symmetry were formed. This result directly implies that the formation energy of the simple perovskite is lower than that of the layered perovskite. It has been recognized that the ionic radius difference between Ba^{2+} (r(XII) = 1.61 Å) and Sm^{3+} (r(XII) = 1.24 Å) leads to cationic ordering in alternating layers of BaO–(Co/Fe)O_2–SmO–(Co/Fe)O_2, forming A-site doped layered perovskite $SmBa(Co/Fe)_2O_{5+\delta}$.[24] In other words, when Sm is able to be doped on A-sites, a layered perovskite instead of a simple perovskite will be formed due to the ionic radius difference between Ba^{2+} and Sm^{3+}. Otherwise, Sm would be doped on the B-sites of the simple perovskite. To further examine this hypothesis, $BaCo_{0.7}Fe_{0.2}Sm_{0.1}O_{3-\delta}$ was synthesized. The XRD pattern shown in Fig. 1b indicates that $BaCo_{0.7}Fe_{0.2}Sm_{0.1}O_{3-\delta}$ is a simple perovskite with cubic symmetry, and no peaks can be found corresponding to the layered perovskite. Combining these results, it is reasonable to assume that when the Sm doping level is relatively small ($x \leq 0.05$), Sm ions tend to dope on the B-sites of nominal composition $Sm_xBa_{1-x}Co_{0.8}Fe_{0.2}O_{3-\delta}$, forming a simple perovskite. When the Sm doping level is relatively high ($x \geq 0.1$), Sm ions tend to dope on both A-sites and B-sites. Sm A-site doping leads to a layered perovskite while the B-site doping creates a simple perovskite. In this situation, a nanocomposite is formed, composed of a layered perovskite and simple perovskite. The simple perovskite could likely be a Ba deficient ABO_3 perovskite according to the nominal composition $Sm_xBa_{1-x}Co_{0.8}Fe_{0.2}O_{3-\delta}$ since Sm goes to the B-site of the simple perovskite. Here, the simple perovskite formed in the nanocomposite is concisely denoted as Ba_{1-y}(Co/Fe/Sm)$O_{3-\delta}$.

To quantitatively determine the compositions of the phases formed in the nanocomposite, further analysis is conducted using Sm10BCF as an example. As observed above, the synthesized nominal composition $Sm_{0.10}Ba_{0.90}Co_{0.8}Fe_{0.2}O_{3-\delta}$ is primarily composed of the simple perovskite Ba_{1-y}(Co/Fe/Sm)$O_{3-\delta}$ and the layered perovskite $SmBa(Co/Fe)_2O_{5+\delta}$. Due to the small amount, the impurity phase of BaO (Fig. 2c) is neglected in the following analysis. To facilitate analysis, the nominal composition $Sm_{0.10}Ba_{0.90}Co_{0.8}Fe_{0.2}O_{3-\delta}$ is simply written as $Sm_{0.10}Ba_{0.90}MO_{3-\delta}$ where M represents the Co/Fe on the B-sites. According to the XRD results mentioned above, the chemical reaction for the synthesis of nominal composition $Sm_{0.10}Ba_{0.90}Co_{0.8}Fe_{0.2}O_{3-\delta}$ can then be expressed as

$$Sm_{0.10}Ba_{0.90}MO_{3-\delta} \rightarrow mBa_{1-y}(M_{1-z}Sm_z)O_{3-\delta} + nSmBaM_2O_{5+\delta} \quad (1)$$

The species conservation of Ba, Sm, and M in (1) directly leads to the following three equations:

$$m^*(1 - y) + n = 0.90 \quad (2)$$

$$m^*z + n = 0.10 \quad (3)$$

$$m^*(1 - z) + 2n = 1 \quad (4)$$

It is obvious that four variables m, y, n, and z need to be determined but only three equations (eqn (2)–(4)) are available. Therefore, one more equation is needed. This equation can be obtained through XRD analysis. In particular, Rietveld refinement was performed on the XRD pattern of the synthesized Sm10BCF using FullProf. For the refinement, the cubic $Pm\bar{3}m$ space group and the orthorhombic $Pmmm$ space group were selected to fit the experimental XRD data. The result is shown in Fig. 3a. The corresponding fitting parameters of refinement are obtained as $\chi^2 = 4.88$, $R_{wp} = 13.3\%$, $R_p = 19.5\%$, and $R_{exp} = 6.04\%$, respectively. Although perfect fitting was not achieved due to the exclusion of the small impurity phase in the

Table 1 Phases contained in Sm*x*BCF nanocomposites

	Simple perovskite		Layered perovskite	Impurity
Sm0BCF	Hexagonal phase	—	—	Fe_3O_4
Sm5BCF	Hexagonal phase	Cubic phase	—	CoO
Sm10BCF	—	Cubic phase	Orthorhombic	BaO
Sm15BCF	Hexagonal phase	Cubic phase	Orthorhombic	—
Sm30BCF	Hexagonal phase	Cubic phase	Orthorhombic	—

Sm10BCF sample and the difficulty in precisely determining the B-site composition, the XRD profile and the fitting results still showed reasonably good agreement overall. Based on the Rietveld refinement results, the mass ratio of the two phases in the synthesized Sm10BCF powders was obtained as

$$\frac{m \times M_{\text{mass, cubic}}}{n \times M_{\text{mass, orthorhombic}}} = \frac{86.87}{13.13} \quad (5)$$

where M_{mass} is the molar mass of the compounds with the subscript self-explained. Combining eqn (2)–(5), we have

$$m = 0.902,\ n = 0.066,\ y = 0.075, \text{ and } z = 0.038$$

This result indicates that the composition of the simple perovskite phase in the nanocomposite Sm10BCF is $Ba_{0.925}(Co/Fe)_{0.962}Sm_{0.038}O_{3-\delta}$ while that of the layered perovskite phase is $SmBa(Co/Fe)_2O_{5+\delta}$. The result also shows that one molar Sm10BCF includes approximately 0.902 molar simple perovskite and 0.066 molar layered perovskite. It is worth mentioning that the above analysis is based on certain simplifications, such as the neglect of impurity phase BaO. Therefore, the composition obtained above might have certain deviations from the true compositions. Nevertheless, as the XRD peak of the impurity phase BaO is very small, such neglect is reasonable and would not affect the major conclusion. The results provide very useful information to quantitatively understand the synthesized nanocomposite with nominal composition Sm10BCF. To further examine the structures of the nanocomposite, a high-resolution TEM image of Sm10BCF powder was obtained and is shown in Fig. 3b. Good crystallization is observed and the two crystals with different fringes are intimately in contact with each other. The two distinct crystal structures exhibit interplanar spacings of 0.264 nm and 0.376 nm, respectively. The plane with an interplanar distance of 0.264 nm closely resembles the (110) plane of $BaCoO_{2.23}$, which has a spacing distance of 0.287 nm. The plane with an interplanar distance of 0.376 nm is close to the (002) plane of $SmBaCo_2O_{5.54}$, which exhibits a spacing distance of 0.389 nm.

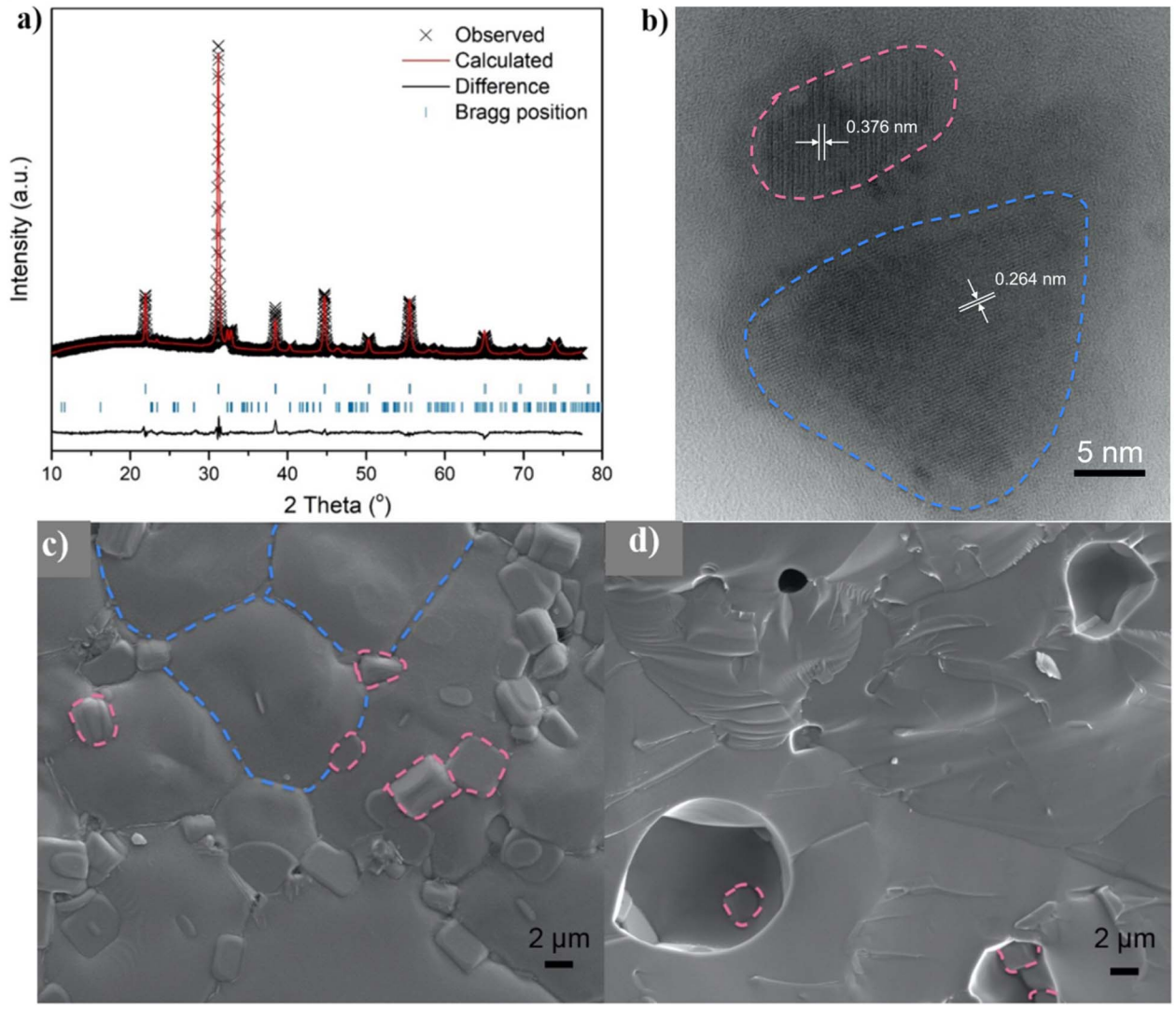

Fig. 3 (a) Refined XRD profiles and (b) high-resolution TEM image of $Sm_{0.10}Ba_{0.90}Co_{0.8}Fe_{0.2}O_{3-\delta}$ powder. (c) Surface and (d) cross-sectional SEM images of bulk Sm10BCF sintered at 1100 °C in air for 6 h.

To further confirm the above analysis, the microstructure and phase distribution in the bulk sample of the Sm10BCF pellet were characterized using SEM in combination with the EDS technique. Fig. 3c and d show the surface and cross-sectional SEM images of bulk Sm10BCF sintered at 1100 °C in air for 6 h, respectively. Grains with two different sizes and very clear boundaries can be observed on the bulk surface (Fig. 3c). Two phases with different grain sizes can also be found in the cross-section SEM image (Fig. 3d), where the phase with the large grain size accounts for a majority part of the bulk while that with the small grain size accounts for a minor amount. The EDS analysis for selected regions indicates that the particles with the large grain size (Fig. 4a) demonstrate a different composition from those with the small grain size (Fig. 4b). The composition of the small particles contains more Sm than the large ones. From the surface and cross-sectional EDS mapping of the Sm10BCF pellet (Fig. 4c and d), it can be clearly seen that the regions covered by small grains show high Sm content and low Ba content, while those covered by large grains demonstrate low Sm and high Ba contents, respectively. These consistent results confirm that the phase of small grains is different from that of large grains and further imply that the large grains are the simple perovskite phase while the small grains are the layered perovskite phase.

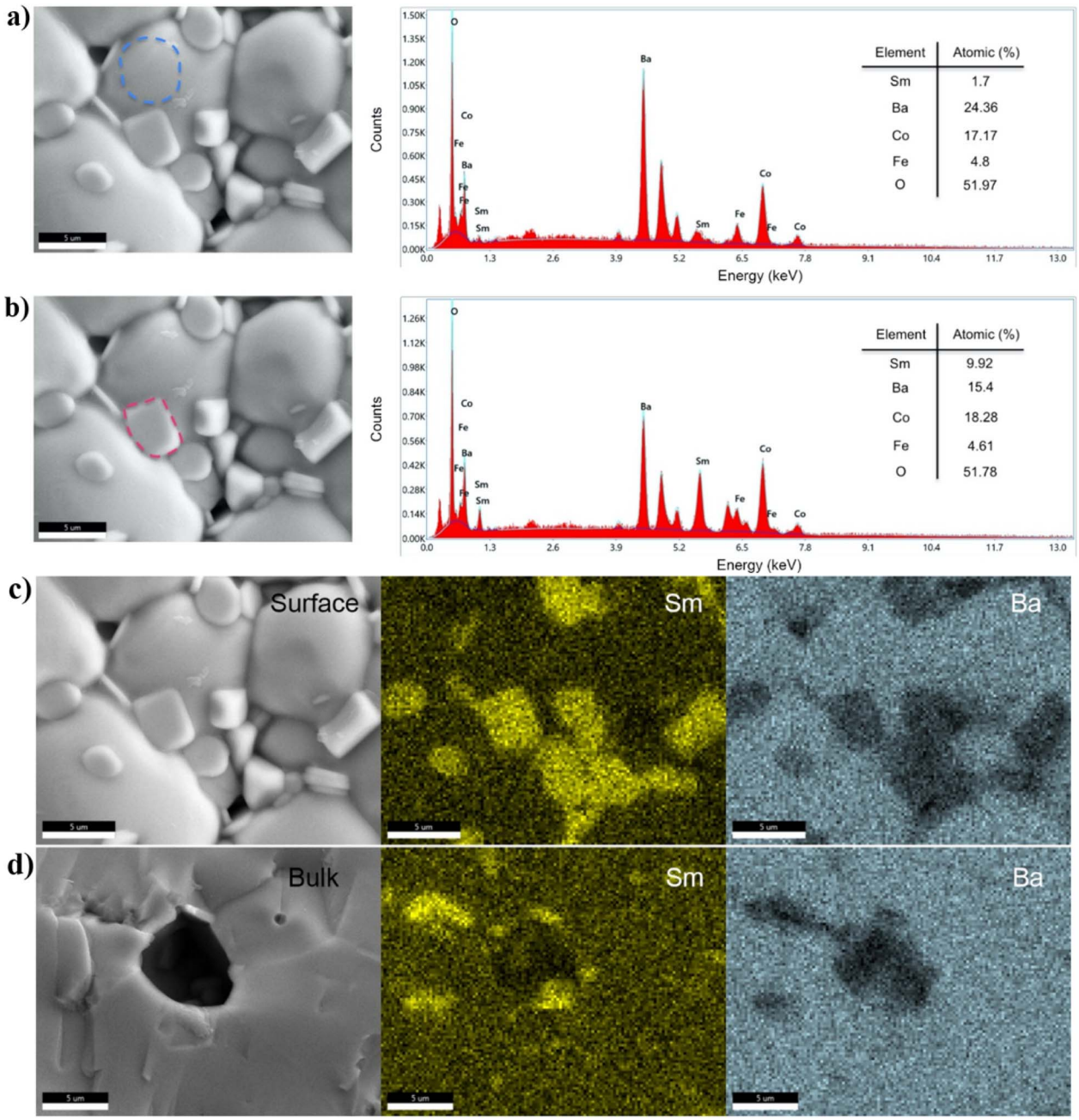

Fig. 4 (a and b) EDS scanning results of the Sm10BCF pellet surface. EDS mapping of the Sm10BCF pellet surface (c) and bulk (d).

3.2 Oxygen reduction reaction activity

The oxygen reduction reaction (ORR) activity of the SmxBCF nanocomposite cathode was characterized using symmetrical cells SmxBCF/SDC/SmxBCF and the EIS technique in a low temperature range of 500–650 °C. Fig. 5a–d shows cross sectional SEM images of the symmetrical cells sintered at 1050 °C in air for 2 h. The particles in the electrodes are well connected, forming porous structures. The electrodes also show intimate contact with dense SDC electrolytes. The typical EIS of the symmetrical cell with the SmxBCF electrode at 650 °C is shown in Fig. 5e, and Fig. 5f shows the frequency response of the imaginary part of the EIS. An equivalent circuit model $L - R_o - (R_hQ_h) - (R_lQ_l)$ (inset of Fig. 5e) was used to fit the EIS data and the fitting results are shown in the same figure. In this model, L is the inductance of the circuit caused by the electrical equipment and lead wires and R_o represents ohmic resistance induced by electrolyte, the electrode backbone and current collecting wires. R_i and Q_i(i = h,l) are the resistance and constant phase capacitance of high (h) and low (l) frequency processes, respectively. The polarization resistance (R_p) of the electrode is then obtained by adding R_h and R_l together.

Fig. 5g shows Arrhenius plots of R_p obtained at 500–650 °C in air for different electrodes and the corresponding activation energy (E_a). For each individual electrode, R_p decreases with increasing operating temperatures, indicating that the polarization process is thermally activated in nature. The electrodes with R_p values ordered from low to high are Sm10BCF, Sm5BCF,

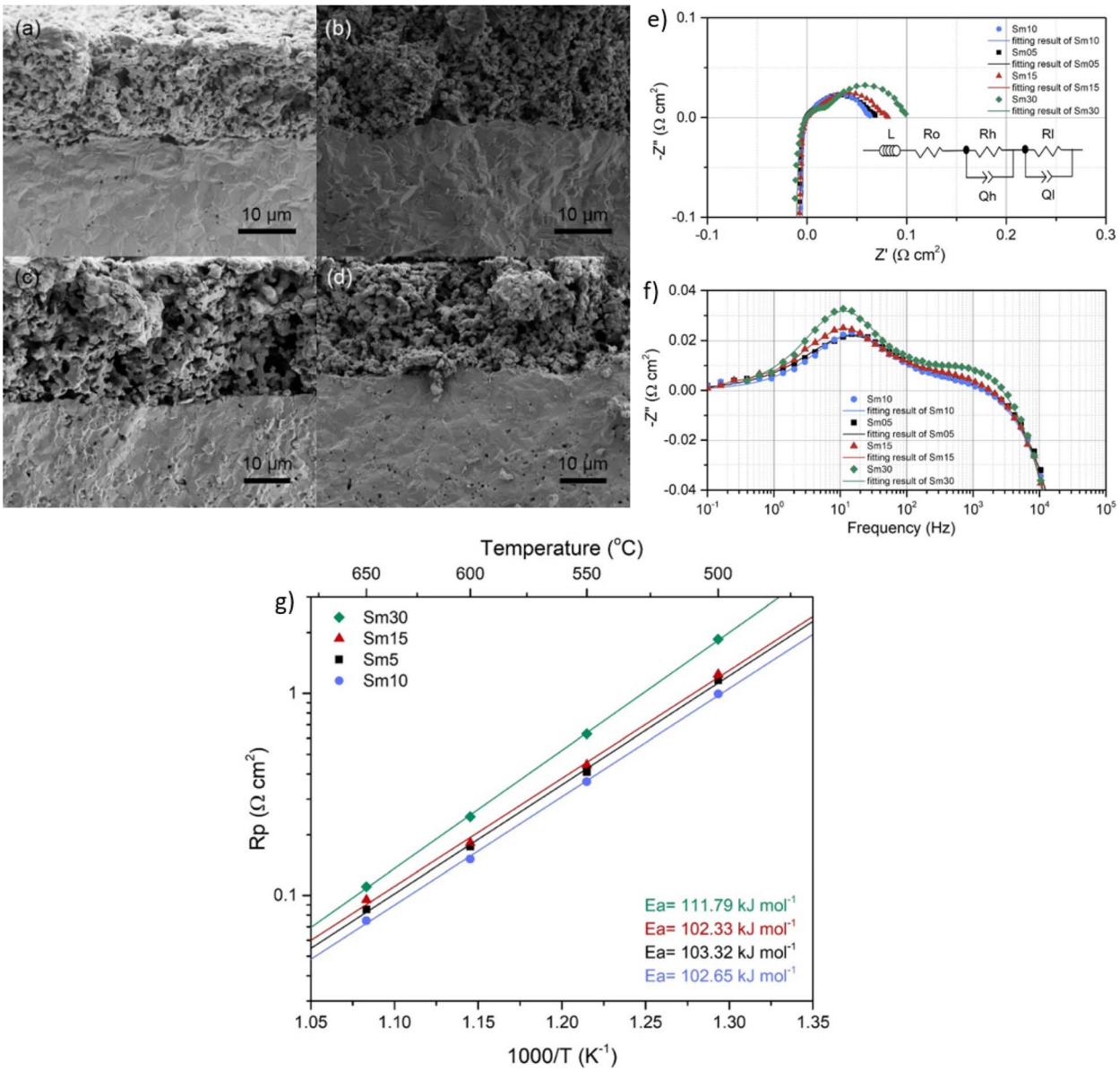

Fig. 5 Cross-sectional SEM images of symmetrical cells with $Sm_xBa_{1-x}Co_{0.8}Fe_{0.2}O_{3-\delta}$ electrodes: (a) Sm5BCF, (b) Sm10BCF, (c) Sm15BCF and (d) Sm30BCF. Typical Nyquist (e) and Bode (f) plots of symmetrical cells with SmxBCF electrodes measured at 650 °C in air. The inset shows an equivalent circuit model used for curve fitting. (g) Polarization resistances *vs.* 1000/T of SmxBCF electrodes measured in air from 500 to 650 °C.

Sm15BCF, and Sm30BCF, respectively, at different temperatures. As mentioned above, the Sm10BCF nanocomposite contains both the simple perovskite with cubic symmetry and layered perovskite with orthorhombic symmetry. The synergy of the cubic perovskite $Ba_{0.925}(Co/Fe)_{0.962}Sm_{0.038}O_{3-\delta}$ and the orthorhombic layered perovskite $SmBa(Co/Fe)_2O_{5+\delta}$ in the Sm10BCF nanocomposite electrode leads to a lower R_p value than the other nanocomposites of Sm5BCF, Sm15BCF, and Sm30BCF electrodes. For example, at 500 °C, the Sm10BCF, Sm5BCF, Sm15BCF, and Sm30BCF electrodes demonstrate R_p values of 0.99, 1.16, 1.24, and 1.85 Ω cm^2 and Sm10BCF electrode shows a 14.7%, 20.2% and 46.5% decrease compared to the other three electrodes, respectively. Fig. 5g also shows that the activation energy of Sm10BCF is 103.32 kJ mol^{-1}, which is similar to those of both Sm5BCF and Sm15BCF but much lower than that of Sm30BCF. The activation energy of Sm10BCF is also much lower than that of the extensively studied BSCF cathode material (116 kJ mol^{-1}).[25] The lower activation energy directly indicates a lower energy barrier for defect hopping, enabling higher electrochemical kinetics for the ORR at reduced temperatures. Therefore, Sm10BCF could be potentially used as a cathode material for low temperature SOFCs.

To better understand the behavior of low polarization resistance associated with the Sm10BCF electrode, the electrode microstructure was further characterized, and the corresponding SEM images are shown in Fig. 6a. Nanoparticles with an average diameter of 30–40 nm are uniformly decorated on the surface of the Sm10BCF porous electrode. The EDS scanning results in Fig. 6c and d show that the composite of the bulk is very close to the surface nanoparticles and the ratio of Ba/(Sm + Co + Fe) in both phases is a little bit less than 1. This observation implies that the bulk and surface nanoparticles could be the same phase of the simple perovskite with A-site deficiency. This result is also consistent with the powder analysis results detailed above, where a majority of the nanocomposite is the simple perovskite with Ba deficient in A-site $Ba_{0.925}$(Co/

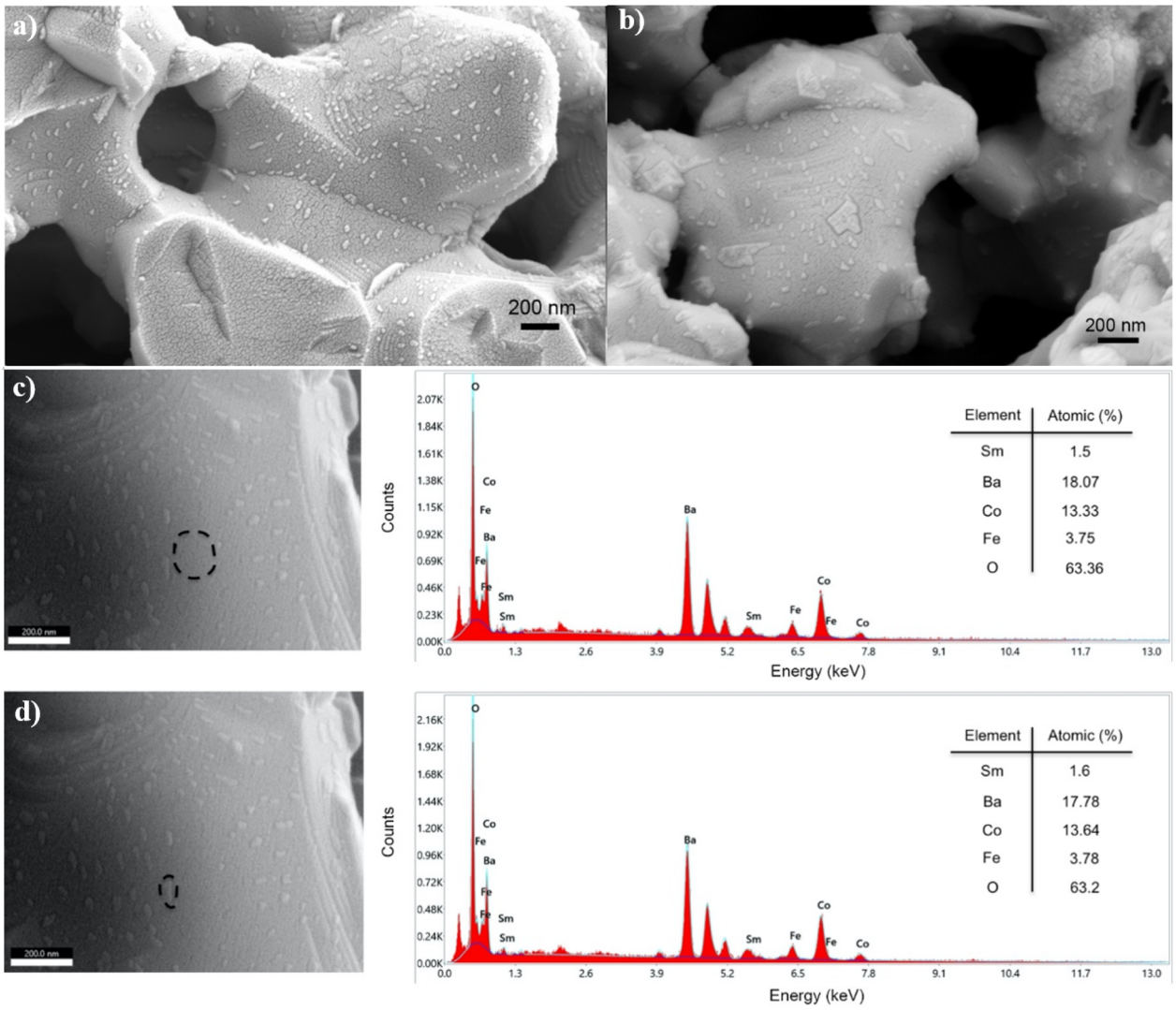

Fig. 6 SEM images of Sm10BCF electrodes calcined at 1050 °C in air for 2 h before (a) and after (b) EIS measurement. The EDS scanning results of the Sm10BCF electrode before EIS measurement, (c) surface and (d) surface nanoparticles.

$Fe)_{0.962}Sm_{0.038}O_{3-\delta}$. In theory, the presence of A-site vacancies in the simple perovskite is not stable thermodynamically and creates a potential to drive the crystal structure toward a stable one, *e.g.*, a stoichiometric simple perovskite with the ratio A/B = 1.[26] This requires that either more Ba elements be doped into the A-site or the elements in the B-site be pushed out of the lattice. Since additional Ba is not available during the sintering process of the Sm10BCF porous electrode, the exsolution of B-site elements could be a reasonable assumption that drives the crystal structure to reach a new equilibrium, and a new surface phase could be formed due to the exsolution of B-site elements. As the EDS results indicated above, the surface nanoparticle demonstrated quite similar composition to the bulk phase. Therefore, the exsolved B-site elements could then be recombined with surface Ba, forming surface nanoparticles of simple perovskite again. As demonstrated in the synthesis part of the nanocomposite, the formation energy of the simple perovskite is lower than that of the layered perovskite. This could be the reason why surface nanoparticles with a simple perovskite structure were formed even though the simple perovskite $Ba_{0.925}(Co/Fe)_{0.962}Sm_{0.038}O_{3-\delta}$ and layered perovskite $SmBa(Co/Fe)_2O_{5+\delta}$ co-exist in the Sm10BCF porous electrode bulk. One also can find that the ratio of Ba/(Co + Fe + Sm) = 0.93 in surface nanoparticles (Fig. 6d) is a little bit lower than 0.97 in the bulk (Fig. 6c). As mentioned above, the A-site deficiency in the simple perovskite creates a potential driving the exsolution of B-site elements so that a new equilibrium can be obtained. The gradients of both surface morphology and element ratios Ba/(Co + Fe + Sm) could be formed to balance such a driving force under the sintering conditions of the Sm10BCF cathode. The surface nanoparticles obviously increase the effective surface area of the porous cathode. This surface feature advantage in combination with the synergetic effect of the cubic simple perovskite and orthorhombic layered perovskite enhances ORR kinetics of Sm10BCF electrodes, leading to the lowest polarization resistance among the Sm*x*BCF nanocomposite electrodes. After the EIS measurement, the microstructure of the symmetrical cell was examined again and is shown in Fig. 6b. Comparing the microstructure before and after the test, no obvious change of morphology can be found, indicating the excellent stability of the Sm10BCF electrode microstructure, especially the surface nanoparticles.

3.3 Electrical conductivity, bulk diffusivity, and surface exchange coefficient of the Sm10BCF nanocomposite

Since Sm10BCF shows the lowest polarization resistance among Sm*x*BCF cathodes, it was further characterized in more detail. Specifically, the electrical conductivity of Sm10BCF was measured using a dense cuboid bar and the four-terminal AC method. Fig. 7a shows the electrical conductivity of the Sm10BCF sample measured in air at different temperatures. Electrical conductivity monotonically increases with increasing temperatures, suggesting the semiconductor behavior of Sm10BCF. At 600 °C, the electrical conductivity of the Sm10BCF nanocomposite reaches 93.24 S cm^{-1}, which is close to the requirement of 100 S cm^{-1} at 600 °C for the cathode of LT-SOFCs. This value is also higher than that of some $BaCoO_3$ based cathode materials for LT-SOFCs.[27] As mentioned before, layered perovskites usually demonstrate much higher electrical conductivity than simple perovskites. The high electrical conductivity of the Sm10BCF nanocomposite could be attributed to the synergy of simple perovskite $Ba_{0.925}(Co/Fe)_{0.962}Sm_{0.038}O_{3-\delta}$ and the layered perovskite $SmBa(Co/Fe)_2O_{5+\delta}$ self-assembled in the nanocomposite.

A mixed conductor of the Sm10BCF nanocomposite involves both electronic and ionic transport processes. Electrical conductivity is primarily contributed by the electronic transport process. To identify the contribution of the ionic transport process, oxygen bulk diffusivity needs to be determined. Also, the ORR activity is closely related to oxygen surface exchange

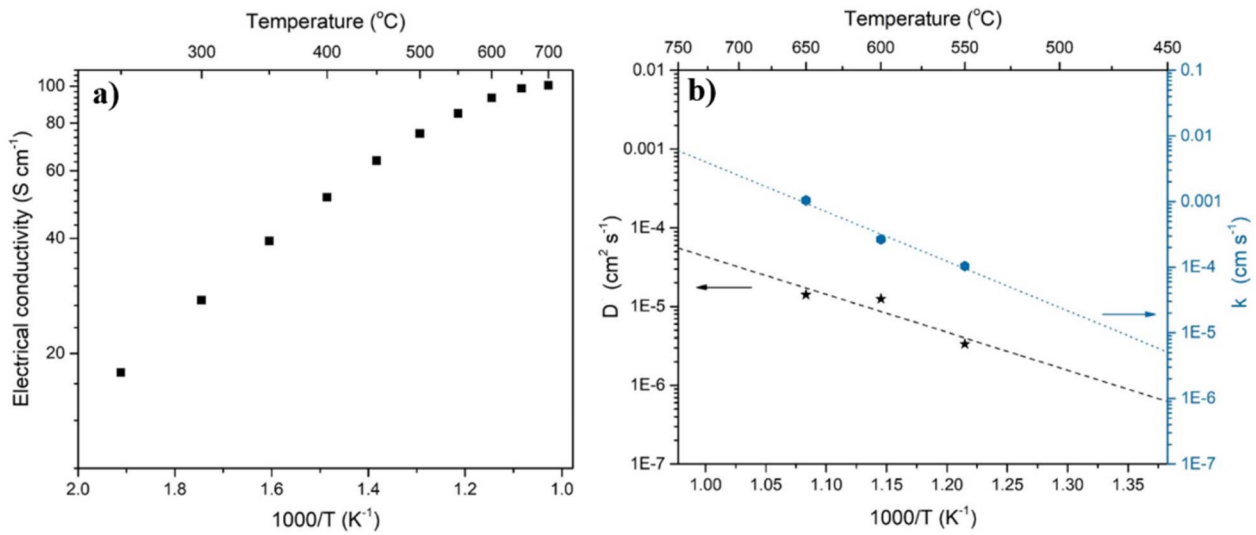

Fig. 7 (a) Temperature dependent electrical conductivity of Sm10BCF. (b) Temperature dependent surface exchange coefficient (*k*) and bulk diffusivity (*D*) of Sm10BCF derived from ECR measurement.

kinetics, quantitatively specified using the surface exchange coefficient. In this section, the bulk diffusivity and surface exchange coefficient of the Sm10BCF nanocomposite are determined using the ECR measurement method. The details of ECR measurement and the analysis algorithm can be found elsewhere.[28,29] Fig. 7b depicts the Arrhenius plots of bulk diffusivity (D) and surface exchange coefficient (k) of Sm10BCF derived from ECR measurement. Both D and k increase with temperatures, indicating the thermally activated nature of ionic transport and surface exchange process. At 600 °C, Sm10BCF demonstrated D and k values of 1.25×10^{-5} cm^2 s^{-1} and 2.66×10^{-4} cm s^{-1}, respectively. These values are in the same order of magnitude as those of the widely studied BSCF material,[26] *i.e.*, 2.5×10^{-5} cm^2 s^{-1} for D and 2.7×10^{-4} cm s^{-1} for k at 600 °C, respectively. One can see that the k values of the two materials are basically the same; the D value of Sm10BCF is a little bit lower than that of BSCF. As mentioned above, Sm10BCF primarily includes the cubic simple perovskite phase $Ba_{0.925}(Co/Fe)_{0.962}Sm_{0.038}O_{3-\delta}$ and a small amount of layered perovskite orthorhombic phase $SmBa(Co/Fe)_2O_{5+\delta}$. The synergy of the two phases in the Sm10BCF nanocomposite determines D and k values.

3.4 Oxygen partial pressure dependent electrochemical kinetics

The multistep reactions involved in the cathodic process are strongly dependent on oxygen pressures applied on the electrode. To obtain more insight into the intrinsic ORR process of the Sm10BCF cathode, polarization resistance of the Sm10BCF cathode was measured using the symmetrical cell with the configuration of Sm10BCF/SDC/Sm10BCF at different oxygen partial pressures and temperatures. The generic relationship between the polarization resistance (R_p) and oxygen partial pressure (P_{O_2}) can be expressed as

$$R_i = k(P_{O_2})^{-m}, \; i = h, l \tag{6}$$

where R is polarization resistance, the subscript i = h,l represents high and low frequency processes, respectively, k is a constant, P_{O_2} is oxygen partial pressure, and m is the reaction order and quantitatively related to rate-limiting steps as follows:[30]

- $m = 1$

$$O_{2,g} + Sm10BCF(s) \leftrightarrow O_{2,ads}(Sm10BCF) \tag{7}$$

The molecular oxygen adsorption process onto the porous electrode surface.

- $m = 0.5$

$$O_{2,ads}(Sm10BCF) \leftrightarrow 2O_{ads}(Sm10BCF) \tag{8}$$

Dissociation of adsorbed molecular oxygen into atomic oxygen.

- $m = 0.25$

$$O_{ads}(Sm10BCF) + 2e^- + V_O^{\cdot\cdot} \leftrightarrow O_O^{\times} + Sm10BCF(s) \tag{9}$$

The charge transfer reaction for oxygen anion formation and incorporation into oxygen vacancies.

- $m = 0$

$$O_{TPB}^{2-} + V_O^{\cdot\cdot}(Sm10BCF\ bulk, Sm10BCF/SDC\ interface) \leftrightarrow O_O^{\times} \tag{10}$$

Oxygen ions transfer within the bulk electrode and/or through the electrolyte/electrode interface.

The polarization resistance (R_p) of the Sm10BCF nanocomposite electrode was obtained using a symmetrical cell and the EIS technique under different oxygen partial pressures (P_{O_2}) and at different temperatures. The high frequency polarization resistance (R_h) and low frequency polarization resistance (R_l) were then extracted from R_p using the curve-fitting technique with an equivalent circuit model. The reaction order m of the

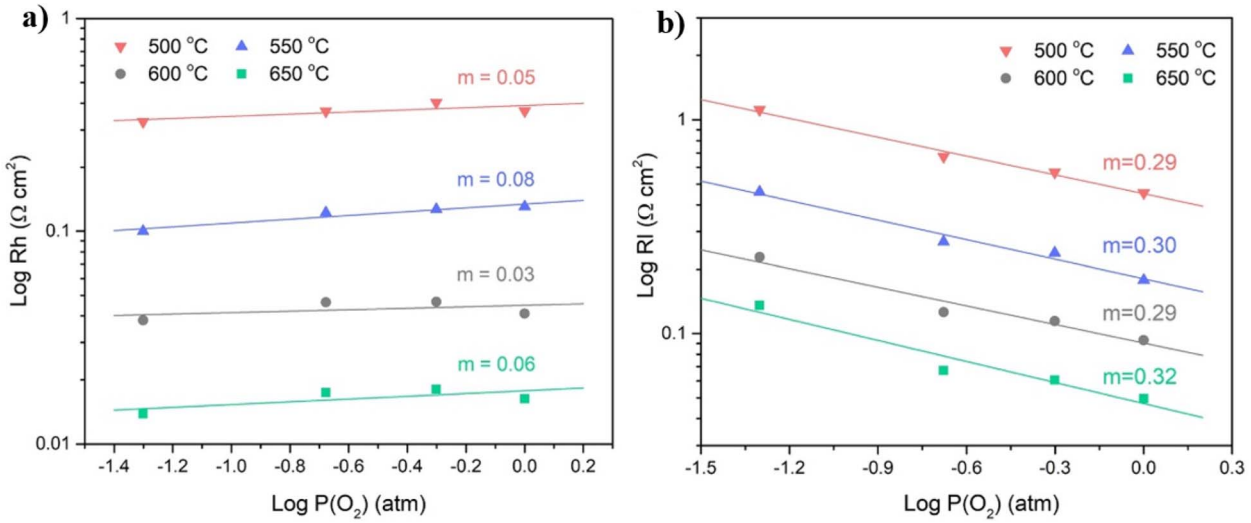

Fig. 8 Correlations between R_1 (a), R_h (b) and applied oxygen partial pressures at different temperatures.

cathodic process was then obtained by curve-fitting on R_h and R_l with respect to the applied oxygen partial pressure. As shown in Fig. 8a, for the high frequency process, the m values are 0.06, 0.03, 0.08 and 0.05 at 650, 600, 550 and 500° C, respectively, which are close to 0. This result indicates that the high frequency process is mainly associated with the oxygen ion transfer process within the bulk electrode and/or through the electrolyte/electrode interface and is very weakly dependent on the applied oxygen partial pressures. For the low frequency process (Fig. 8b), the slope m values of 0.32, 0.29, 0.30 and 0.29 were obtained at 650, 600, 550 and 500° C, respectively, which are close to 0.25. Therefore, the low frequency process could be related to the charge transfer process. One can also notice that R_l is much larger than R_h in the whole range of operating conditions, indicating that the charge transfer process is the major rate-limiting step in the ORR of the Sm10BCF cathode.

3.5 Stability test with the symmetrical cell

The stability of a cathode material is critical for practical applications of SOFCs. In this section, the stability of the Sm10BCF nanocomposite cathode was studied at 600 °C in air for ~192 h using a symmetrical cell Sm10BCF/SDC/Sm10BCF. The EIS was measured periodically during the test and overall polarization resistance (R_p) of the electrode was obtained from EIS data. Fig. 9a shows the time history of the polarization resistance R_p. It can be seen that R_p asymptotically increased in the first 49 hours, beyond which it remained relatively stable. To better understand the fundamental mechanism of Sm10BCF electrode degradation, the polarization resistances of high frequency (R_h) and low frequency (R_l) processes were extracted from the overall polarization resistance (R_p). Fig. 9b and c show the time history of R_h and R_l, respectively. Obviously, R_h remained relatively stable during the 192-hour test. Since the high frequency polarization is associated with oxygen ion transport within the bulk electrode and/or through the electrolyte/electrode interface, it is reasonable to assume that no obvious degradations occurred within the bulk electrode and/or at electrode/electrolyte interfaces. These may include defect distributions and grains/grain boundaries within the bulk and microstructures of porous electrodes. The polarization of the low frequency process followed a similar trend to the overall polarization resistance, asymptotically increasing in the first 49 hours but remaining relatively stable beyond the 49 hours. As mentioned above, the low frequency process is closely related to the charge transfer process, which involves the formation of oxygen anions and incorporation into oxygen vacancies. Certainly, this process is strongly dependent on the characteristics of the bulk electrode surface, such as electro/catalytic properties and distribution of oxygen vacancies. The increase in R_l in the first 49 hours might be induced by aging and reorganization of surface features. These may include the evolution of nanoparticles decorated on the surface, oxygen vacancy redistribution, and possible segregation of surface cation Ba^{2+}.[31] Once stabilized, the R_l remained relatively stable during the test beyond the first 49 hours. Fig. 9d shows a SEM image of the Sm10BCF electrode in the symmetrical cell after the stability test. Obviously, uniform nanoparticles are still observable on the surface of the electrode. Compared to the electrode before the test (Fig. 6a), where the surface nanoparticle size is ~30–40 nm, the surface nanoparticles after the stability test became large and reached a diameter of ~100 nm, implying that nanoparticles were agglomerated during the stability test. It is also noticed that the surface nanoparticles tended to appear near grain boundaries. The EDS scanning analysis indicates that the surface nanoparticles are Co-rich phase (Fig. 9e), particularly at the tip of the nanoparticles (Fig. 9f). It is worth mentioning that polarization resistance of electrodes in a long-term symmetrical cell test only reflects, to a large extent, the thermal stability of the electrode. To understand the stability of the cathode under practical conditions, a single cell test is needed. This typically includes the stability of electrode materials under various current loads, especially large current loading conditions.

3.6 Single-cell performance and stability

Single cells provide a flexible platform to examine the performance of cathode materials under practical operating conditions. In this section, an anode-supported button cell NiO-SDC/SDC/Sm10BCF was employed to evaluate electrochemical performance and stability of the Sm10BCF nanocomposite cathode. Fig. 10a shows the I–V and I–P curves of the cell over the operating temperature range of 550–650 °C when humidified hydrogen was used as fuel and ambient air was used as an oxidant. The corresponding EIS under open circuit voltage (OCV) conditions are shown in Fig. 10b. The OCV of the cell reached 0.74, 0.78, and 0.79 V at 650, 600 and 550 °C, respectively. In the anode-supported button cell prepared in this study, the thickness of the SDC electrolyte is only about 12 μm (Fig. 10c). It is well-known that electronic leakage exists in SDC electrolyte.[32] These are the major reasons leading to lower OCVs than the theoretical ones. Peak power densities of 1271, 965, and 572 mW cm^{-2} were obtained at 650, 600 and 550 °C, respectively. The electrochemical performance demonstrated here is among the best of LT-SOFCs, implying that the Sm10BCF nanocomposite is a good candidate for low temperature cathodes. The cross-sectional SEM image of the post-test button cell in Fig. 10c indicates that the cathode and anode are well adhered to the electrolyte and show uniform porosity. The electrolyte is dense with some close pores.

A long-term stability test of the Sm10BCF cathode was conducted using the anode-supported button cell. In particular, the operating temperature of the cell was controlled at 600 °C. A current density load of 600 mA cm^{-2} was applied to the cell and the corresponding cell voltage was measured. The experiment under these conditions lasted for about 333 h. Fig. 11a shows the time history of the cell voltage response. Except for the first ~25 h during which the cell voltage showed a slight asymptotic decrease, the rest of the voltage time history was very stable. This observation indicates that the material system of the cell might take a little time (~25 h) to stabilize, *e.g.*, the microstructure and/or defects took time to reach an equilibrium. Once stabilized, the performance was very stable during the rest

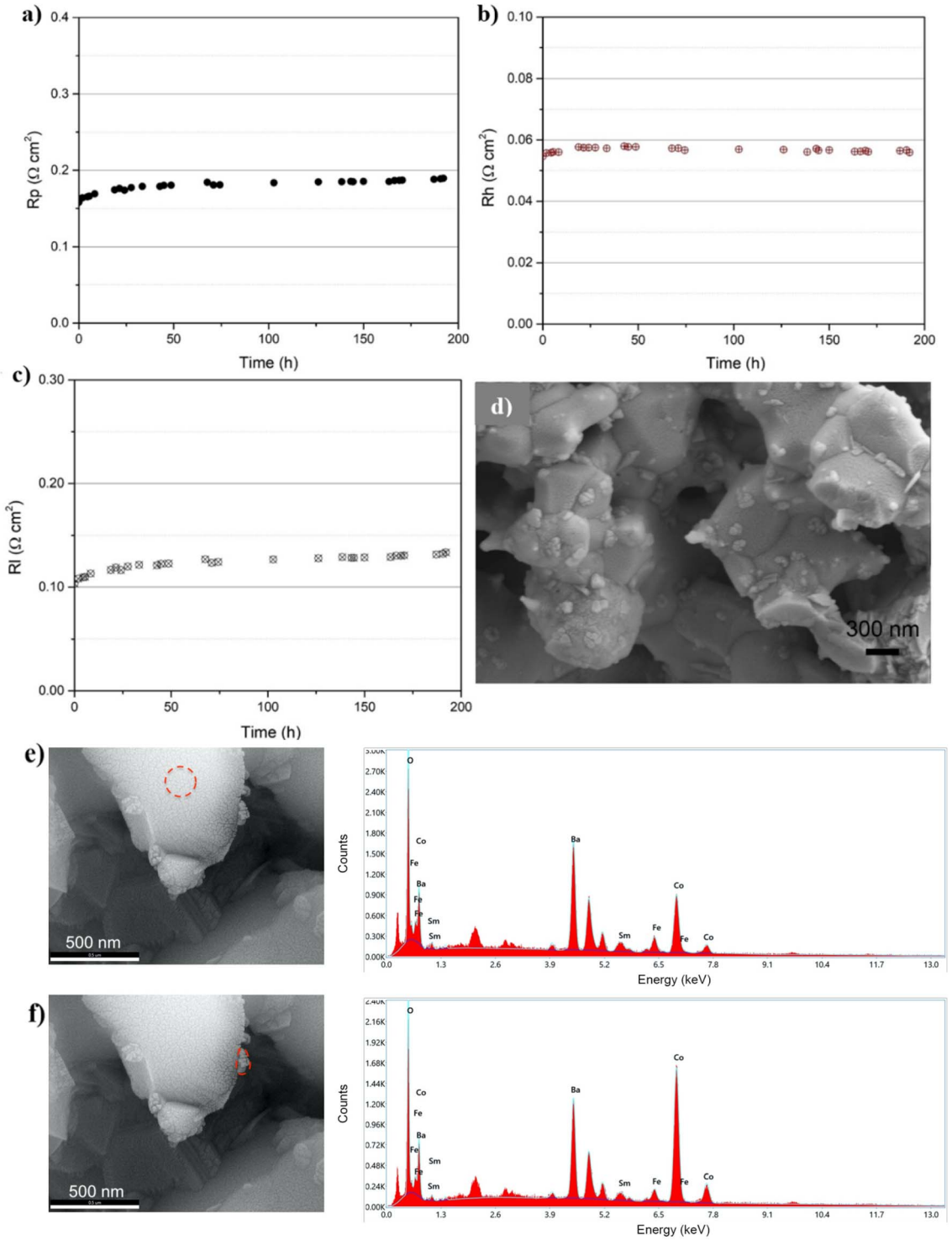

Fig. 9 (a) Time history of polarization resistance Rp of symmetrical cell Sm10BCF|SDC|Sm10BCF at 600 °C in air for a 192 h stability test; time history of Sm10BCF cathode polarization resistance associated with (b) high frequency process and (c) low frequency process derived from R_p; (d) SEM image of the Sm10BCF electrode in the symmetrical cell after the stability test; (e) surface and (f) tip of surface nanoparticles; the EDS scanning results of the Sm10BCF cathode after the symmetrical cell stability test.

of the long-term test. Obviously, the Sm10BCF nanocomposite cathode demonstrated not only very good electrochemical performance but also reasonably good long-term stability.

To examine the stability of the Sm10BCF nanocomposite cathode under extremely large current density loads, the current density load was changed between 600 and 1700 mA cm^{-2} every 2 hours at 600 °C. The corresponding cell voltage was measured. The stability test was conducted for ~16 h under such conditions. Fig. 11b shows the time history of cell voltage response. Cell voltage showed rapid changes when the current density

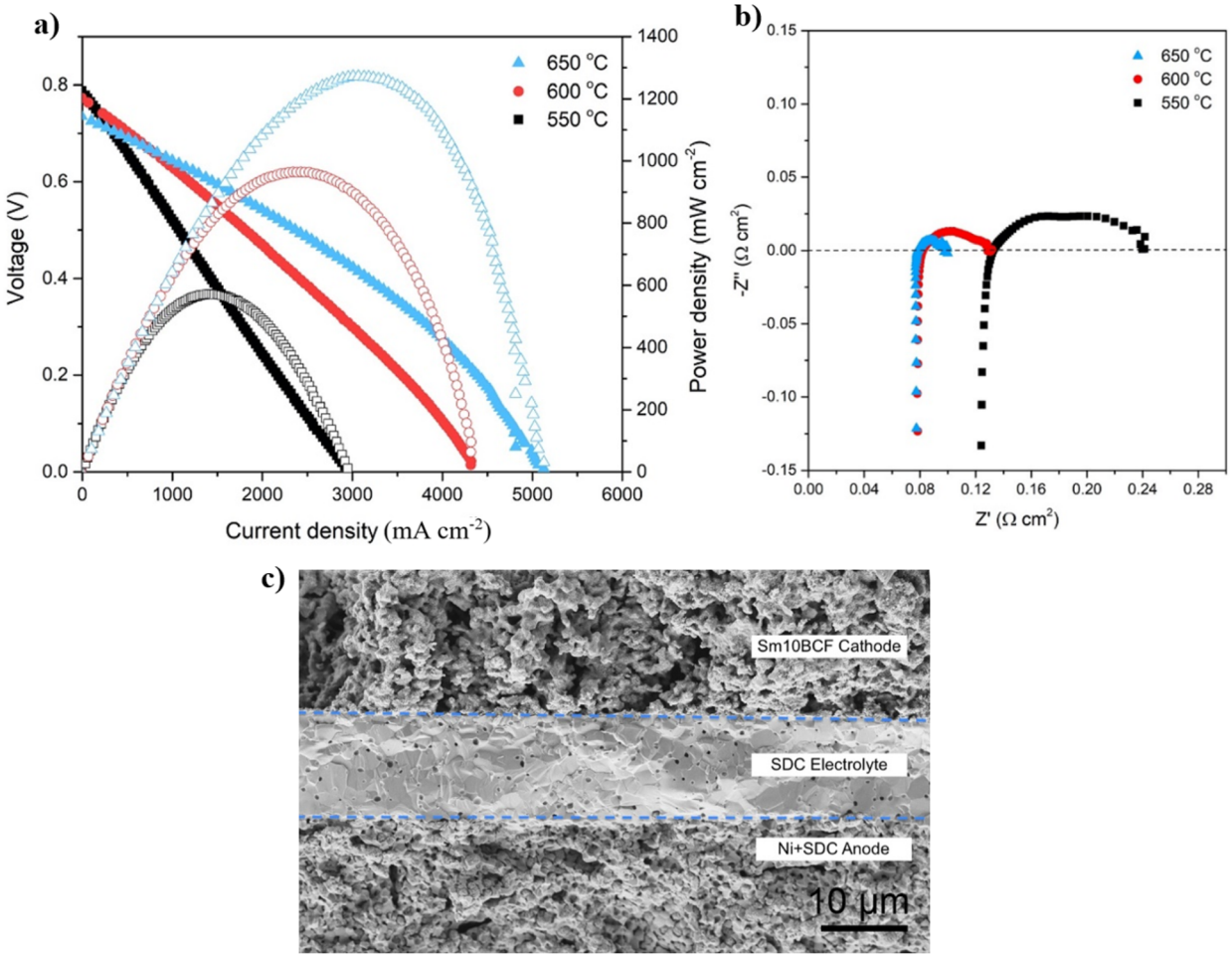

Fig. 10 (a) *I*–*V* and *I*–*P* curves and (b) EIS curves under OCV conditions of the anode supported cell with the configuration of Sm10BCF/SDC/NiO + SDC at temperatures of 550–650 °C; (c) cross-sectional SEM image of the cell after the electrochemical test.

load was switched between 600 and 1700 mA cm^{-2}. After a few cycles of current loading changes, the cell voltage did not show any obvious degradation, indicating that the cell performance can be readily recovered under very large current loading conditions. The results further imply the excellent stability of the Sm10BCF nanocomposite cathode under large current loads. The electrochemical performance and stability demonstrated above suggest that the Sm10BCF nanocomposite is a great cathode candidate for high performance and durable LT-SOFCs.

In the stability test with the symmetrical cell demonstrated above, the major external load is the thermal load. The SEM images of the Sm10BCF electrode before and after the stability test show that the surface nanoparticles increased from 30–40 nm (Fig. 6a) to ~100 nm (Fig. 9d) and the area density of surface nanoparticles (the number of nanoparticles per unit area) decreased. This result directly implies that the thermal load drove the evolution of microstructures, leading to the agglomeration of surface nanoparticles. In the stability test of the anode-supported button cell, both thermal load and current load were applied to the Sm10BCF nanocomposite electrode. On comparing the SEM image in Fig. 11d with that in Fig. 9d, one may find that the nanoparticle size further increased (80–150 nm); meanwhile, the area density of surface nanoparticles decreased. Since the symmetrical cell was primarily subject to the thermal load while both thermal load and current load were applied to the single cell, it is reasonable to assume that the current load led to further evolution of the electrode morphology. Therefore, the current load is another force driving the coalescence and agglomeration of surface nanoparticles. It is also noticed that surface nanoparticles tend to agglomerate near the grain boundaries especially for the cathode in the single cell under a long-term large current load.

The element content in surface nanoparticles of the post-test button cell was further characterized using the EDS technique. For the selected nanoparticles bonded on the grain surface, the element content is shown in Fig. 11e, while those at the grain boundary are shown in Fig. 11f. The nanoparticles on the grain surface are a Co-rich phase and the ones at the grain boundary contain even higher Co-content. Several factors could play important roles in the evolution of element content and morphology of surface nanoparticles. As mentioned above, the simple perovskite in the Sm10BCF nanocomposite is an A-site Ba cation deficient oxide. The thermodynamic effect and the

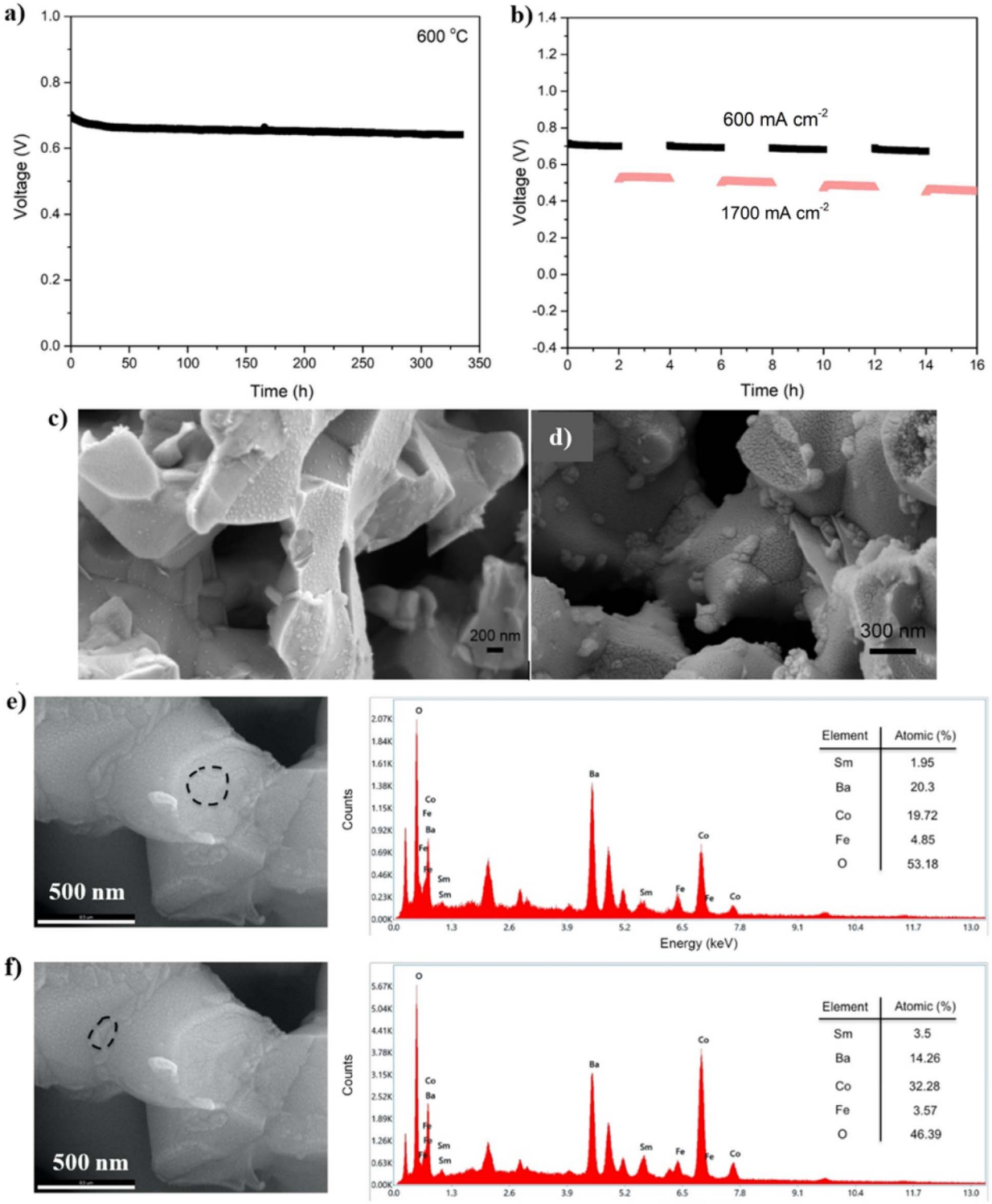

Fig. 11 Stability test of anode-supported cell Ni-SDC/SDC/Sm10BCF under (a) a constant current density load of 600 mA cm^{-2} and (b) large alternating current density load between 600 and 1700 mA cm^{-2} at 600 °C; SEM images of the Sm10BCF cathode before (c) and after (d) the stability test; (e) and (f) EDS scanning results of the Sm10BCF cathode after the stability test.

oxygen ionic incorporation process at the solid/gas interface create a driving force that could vibrantly drive the exsolution of B-site elements from their parent perovskite oxide. As a result, the Co content of the nanoparticles obviously increased compared to the as-fabricated one (Fig. 6c and d). On comparing Fig. 9e and f and Fig. 11e and f, one can see that the Co contents in the corresponding surface nanoparticles are very close. This observation implies that the surface charge (oxygen ions) transfer has a negligible effect on Co content of surface nanoparticles and the thermodynamic effect plays a major role

in this regard. On the other hand, nanoparticles have high surface energy. This high surface energy in turn creates a potential that also drives the coalescence and agglomeration of the nanoparticles under the long-term thermal and large current loading conditions. The Co-rich nanoparticles may enhance the ORR activity of the cathode, leading to favorable electrochemical performance as demonstrated above. While the aggregation of surface nanoparticles could affect the stability of the cathode especially at the initial stage of the durability test, the long-term stability test indicated that the single cell exhibited excellent durability performance. This implies that aggregation of surface nanoparticles reaches an equilibrium after the initial evolution stage. The experimental results suggest that the Sm10BCF nanocomposite is a great candidate for ORR electrocatalysts for LT-SOFC applications.

4 Conclusion

A family of materials with nominal composition $Sm_xBa_{1-x}Co_{0.8}Fe_{0.2}O_{3-\delta}$ ($x = 0$, 0.05, 0.10, 0.15 and 0.30) were synthesized and nanocomposites were formed *via* a one-pot synthesis route. Depending on Sm doping levels, the nanocomposite primarily consists of a simple perovskite and/or layered perovskite with different phases. The nanocomposite with nominal composition $Sm_{0.10}Ba_{0.90}Co_{0.8}Fe_{0.2}O_{3-\delta}$ (Sm10BCF) is composed primarily of a cubic phase of Ba deficient ABO_3 simple perovskite $Ba_{0.925}(Co/Fe)_{0.962}Sm_{0.038}O_{3-\delta}$ and a layered perovskite with orthorhombic symmetry $SmBa(Co/Fe)_2O_{5+\delta}$ and demonstrated electrochemical performance comparable to that of the best cathode materials in open literature. The nanocomposite Sm10BCF also showed very good stability as an electrode material in a symmetrical cell in a ~192 h durability test at 600 °C. It was also able to self-assemble nanoparticles uniformly decorated on the Sm10BCF cathode surface in a one-step sintering process. The corresponding anode-supported button cell delivered a peak power density of 1271 mW cm^{-2} at 650 °C and demonstrated excellent stability over ~333 h at a constant current density of 600 mA cm^{-2} at 600 °C. The anode-supported button cell was also able to sustain stable performance under extremely large current loads step-varying between 600 and 1700 mA cm^{-2} alternately. The composition of surface nanoparticles in the as-fabricated cathode is quite similar to that of the simple perovskite substrate. During the long-term stability test, the surface nanoparticles showed a slight agglomeration, forming relatively large surface nanoparticles with less area density. The nanoparticles tended to agglomerate around grain boundaries and appeared to be having Co-rich phases. Three driving forces primarily contributed to the evolution of surface nanoparticles, including thermal force, applied current loading and high surface energy of nanoparticles. After an initial evolution of surface nanoparticles, the morphology of the cathode reached a new stable equilibrium, which was confirmed by the stable cell performance during the long term durability test. This research provides an efficient and cost-effective route to prepare perovskite nanocomposites and surface nanoparticle-decorated cathodes for high performance and durable LT-SOFCs.

Data availability

The authors confirm that the data supporting the findings of this study are available within the article.

Conflicts of interest

There are no conflicts of interest to declare.

Acknowledgements

Much of the material was converted from the first author's dissertation entitled “Exploration and Evaluation of Novel Cathode Materials for Intermediate-to-Low Temperature Solid Oxide Fuel Cells”, University of South Carolina, 2020.

References

1 N. Q. Minh, *J. Am. Ceram. Soc.*, 1993, **76**, 563–588.
2 B. C. Steele and A. Heinzel, in *Materials for Sustainable Energy: A Collection of Peer-Reviewed Research and Review Articles from Nature Publishing Group*, World Scientific, 2011, pp. 224–231.
3 C. Graves, S. D. Ebbesen, S. H. Jensen, S. B. Simonsen and M. B. Mogensen, *Nat. Mater.*, 2015, **14**, 239–244.
4 Y. Zhang, R. Knibbe, J. Sunarso, Y. Zhong, W. Zhou, Z. Shao and Z. Zhu, *Adv. Mater.*, 2017, **29**, 1700132.
5 E. D. Wachsman and K. T. Lee, *Science*, 2011, **334**, 935–939.
6 L. Yang, S. Wang, K. Blinn, M. Liu, Z. Liu, Z. Cheng and M. Liu, *Science*, 2009, **326**, 126–129.
7 Z. Gao, L. V. Mogni, E. C. Miller, J. G. Railsback and S. A. Barnett, *Energy Environ. Sci.*, 2016, **9**, 1602–1644.
8 Y.-L. Huang, A. M. Hussain, I. A. Robinson and E. D. Wachsman, *ACS Appl. Mater. Interfaces*, 2018, **10**, 28635–28643.
9 C. Yang, Y. Gan, M. Lee, C. Ren and X. Xue, *J. Electrochem. Soc.*, 2018, **165**(13), F1032–F1042.
10 C. Yang, Y. Gan, M. Lee, C. Ren, K. Brinkman, R. D. Green and X. Xue, *J. Mater. Chem. A*, 2020, **8**(20), 10450–10461.
11 Z. Shao and S. M. Haile, *Nature*, 2004, **431**, 170.
12 W. Zhou, R. Ran, Z. Shao, W. Jin and N. Xu, *J. Power Sources*, 2008, **182**, 24.
13 D. Marrero-López, R. Romero, F. Martín and J. Ramos-Barrado, *J. Power Sources*, 2014, **255**, 308.
14 F. Wang, D. Chen and Z. Shao, *Electrochim. Acta*, 2013, **103**, 23–31.
15 X. Kuai, G. Yang, Y. Chen, H. Sun, J. Dai, Y. Song, R. Ran, W. Wang, W. Zhou and Z. Shao, *Adv. Energy Mater.*, 2019, **9**, 1902384.
16 J.-H. Kim and A. Manthiram, *J. Electrochem. Soc.*, 2008, **155**, B385.
17 A. Jun, J. Kim, J. Shin and G. Kim, *Int. J. Hydrogen Energy*, 2012, **37**, 18381–18388.
18 D. Ding, X. Li, S. Y. Lai, K. Gerdes and M. Liu, *Energy Environ. Sci.*, 2014, **7**, 552–575.

19 Y. Guo, S. Wang, R. Li, J. Yu, X. Zhang, M. Li, X. Zheng, J. Zhu, Y. Song, G. Wang and X. Bao, *Joule*, 2024, **8**(7), 2016–2032.
20 Y. Zhu, W. Zhou, R. Ran, Y. Chen, Z. Shao and M. Liu, *Nano Lett.*, 2016, **16**, 512–518.
21 Z. Liu, Y. Bai, H. Sun, D. Guan, W. Li, W.-H. Huang, P. Chih-Wen, Z. Hu, G. Yang, Y. Zhu, R. Ran, W. Zhou and Z. Shao, *Nat. Commun.*, 2024, **15**, 472.
22 Z. Liu, Y. Lin, H. Nie, D. Liu, Y. Li, X. Zhao, T. Li, G. Yang, Y. Sun, Y. Zhu, W. Wang, R. Ran, W. Zhou and Z. Shao, *Adv. Funct. Mater.*, 2024, **34**, 2311140.
23 F. Ciucci, *Solid State Ionics*, 2013, **239**, 28–40.
24 R. D. Shannon, *Acta Crystallogr. Sect. A Cryst. Phys. Diffr. Theor. Gen. Crystallogr.*, 1976, **32**, 751–767.
25 Z. Shao and S. M. Haile, in *Materials for Sustainable Energy: A Collection of Peer-Reviewed Research and Review Articles from Nature Publishing Group*, World Scientific, 2011, pp. 255–258.
26 D. Chen and Z. Shao, *Int. J. Hydrogen Energy*, 2011, **36**, 6948–6956.
27 R. Vinoth Kumar and A. P. Khandale, *Renew. Sustain. Energy Rev.*, 2022, **156**, 111985.
28 F. He, X. Jin, T. Tian, H. Ding, R. D. Green and X. Xue, *J. Electrochem. Soc.*, 2015, **162**(9), F951–F958.
29 F. He, Y. Jiang, C. Ren, G. Dong, Y. Gan, M. Lee, R. D. Green and X. Xue, *Solid State Ionics*, 2016, **297**, 82–92.
30 M. Escudero, A. Aguadero, J. A. Alonso and L. Daza, *J. Electroanal. Chem.*, 2007, **611**, 107–116.
31 Y. Li, W. Zhang, Y. Zheng, J. Chen, B. Yu, Y. Chen and M. Liu, *Chem. Soc. Rev.*, 2017, **46**, 6345–6378.
32 Q. Zhou, Y. Zhang, Y. Shen and T. He, *J. Electrochem. Soc.*, 2010, **157**(5), B628–B632.